





Internal Wave Imprints on Temperature Fluctuations as Revealed by Rapid-Sampling Deep Profiling Floats

Zhiyuan Gao^{1,2} , Zhaohui Chen^{1,2} , Xiaodong Huang^{1,2}, Zhenhua Xu^{2,3} , Haiyuan Yang^{1,2} , Zhongsheng Zhao^{1,2}, Chong Ren², and Lixin Wu^{1,2}

¹Key Laboratory of Physical Oceanography/Institute for Advanced Ocean Science/Frontiers Science Center for Deep Ocean Multispheres and Earth System, Ocean University of China, Qingdao, China, ²Pilot National Laboratory for Marine Science and Technology (Qingdao), Qingdao, China, ³Key Laboratory of Ocean Circulation and Waves, Institute of Oceanology, Chinese Academy of Sciences, Qingdao, China

Key Points:

- Internal waves are found to have considerable imprints on temperature fluctuations using rapid-sampling deep profiling floats
- The temperature fluctuations can reach 7 m °C at 4,000 m, posing challenges to assess the real deep ocean warming rate
- The internal waves induced temperature fluctuations in the deep ocean are generally larger in the Philippine Basin and Mariana Arc

Correspondence to:

Z. Chen,
chenzhaohui@ouc.edu.cn

Citation:

Gao, Z., Chen, Z., Huang, X., Xu, Z., Yang, H., Zhao, Z., et al. (2021). Internal wave imprints on temperature fluctuations as revealed by rapid-sampling deep profiling floats. *Journal of Geophysical Research: Oceans*, 126, e2021JC017878. <https://doi.org/10.1029/2021JC017878>

Received 9 AUG 2021
Accepted 9 DEC 2021

Abstract Internal waves play important roles in modulating the temperature variations and heat transfers in stratified oceans. However, due to the deep ocean measuring approach limitations, it is still challengeable to characterize the temperature fluctuations induced by internal waves in the deep oceans below 2,000 m. In this study, a fleet of rapid-sampling deep profiling floats with an approximately daily sampling rate was deployed in the northeastern South China Sea (SCS), Philippine Basin (PB), Mariana Arc (MA), and Kuroshio Extension (KE). Results show that the internal waves, internal tides or near-inertial waves, have considerable imprints on local temperature fluctuations. Geographically, the internal wave induced temperature fluctuations are generally larger in the PB and MA, indicative of a strong deep signature of internal tides generated by local energetic tide-topography interactions or radiation from remote sources. The temperature fluctuations at 4,000 m can reach up to 7 m°C in most regions, which may cover up real signals of temperature change, posing challenges to assess the deep ocean warming rate through currently insufficient deep profiling floats. Besides, the amplitude of isopycnal displacement in the PB and MA is evidently larger than in KE at 4,000 m, which implies enhanced diapycnal diffusivity and mixing in the deep layers of open oceans with rough topography.

Plain Language Summary Internal waves are ubiquitous in the global ocean, and their propagations are accompanied by the rise and falls of isopycnals which induce fluctuations in local temperature. However, in situ observations of high-frequency temperature fluctuations in the deep ocean are still insufficient. Here we used a fleet of rapid-sampling deep profiling floats to assess the temperature fluctuations induced by internal waves. We found that the magnitude of internal wave induced deep ocean temperature fluctuations is evidently stronger than the long-term trend, especially in the Philippine Basin (PB) and Mariana Arc (MA) with rough topography. Therefore, a more cautious approach should be used to assess the deep ocean warming rate in areas with strong internal waves.

1. Introduction

The two-decade Argo array has been the most successful ocean observation network in the 21st century. Nearly 4,000 profiling floats, covering the ice-free oceans, have sustained continuous observations of temperature and salinity from the sea surface to 2,000 m and provided unprecedented data distributed in the global ocean (Roemmich, Alford, et al., 2019). Over 2 million profiles of upper ocean measurements have significantly broadened our scopes of multiscale oceanic processes (Busecke & Abernathey, 2019; Chen et al., 2017; Durack et al., 2012; Johnson et al., 2016; Matthews et al., 2007; Wu et al., 2011) and offered new insights into ocean circulation and climate change (Cheng et al., 2019; Campbell et al., 2019; Roemmich et al., 2012; Gleckler et al., 2016), oceanic mesoscale eddies (Dufois et al., 2016; Zhang et al., 2014), water mass and mode water (Xu, Li, et al., 2016), and so forth.

In addition to large-scale circulation and mesoscale processes, small-scale/short-term processes like oceanic internal waves can also be identified and assessed regarding their impacts on temperature by repeated measurements of core-Argo floats, which commonly profile the upper 2,000 m ocean in 10-day repeated cycle. The typical timescales of internal waves (internal tides and near-inertial waves) are hours to days, much shorter than the conventional sampling period of Argo floats. Nevertheless, a recent study by Hennon et al. (2019) suggests that internal tides can be appropriately identified and resolved based on temperature anomalies obtained by

© 2021 The Authors.

This is an open access article under the terms of the [Creative Commons Attribution-NonCommercial License](https://creativecommons.org/licenses/by/4.0/), which permits use, distribution and reproduction in any medium, provided the original work is properly cited and is not used for commercial purposes.

Table 1
Information of 10 Deep Profiling Floats Deployed in 2019

No.	Date of deployment	Location of deployment	Area of profiling	Date of termination	Cycle count	CTD model	Prototype model
#1	May 11, 2019	114.98°E 18.10°N	114.97°–115.81°E 17.99°–18.90°N	August 11, 2019	122	SBE-37	OUC ^a
#2	August 5, 2019	124.55°E 18.99°N	123.38°–124.96°E 18.99°–20.16°N	December 10, 2019	131	SBE-37	HM4000 ^b
#3	August 5, 2019	124.58°E 19.10°N	124.03°–124.99°E 19.10°–20.24°N	December 11, 2019	132	SBE-37	HM4000
#4	November 17, 2019	150.00°E 16.01°N	148.22°–150.01°E 16.01°–17.96°N	March 14, 2020	124	SBE-37	OUC
#5	September 10, 2019	152.28°E 37.87°N	148.19°–154.00°E 36.54°–38.33°N	January 24, 2020	140	SBE-37	OUC
#6	August 4, 2019	124.67°E 19.08°N	123.36°–124.76°E 18.78°–19.26°N	December 12, 2019	115	SBE-37	OUC
#7	November 8, 2019	149.85°E 40.07°N	149.28°–156.16°E 40.07°–44.35°N	April 28, 2020	176	SBE-37	OUC
#8	August 5, 2019	124.60°E 19.11°N	124.33°–124.96°E 19.08°–19.44°N	September 27, 2019	53	SBE-37	HM4000
#9	August 5, 2019	124.63°E 19.09°N	124.32°–124.87°E 19.09°–19.45°N	September 19, 2019	55	SBE-37	HM4000
#10	August 5, 2019	124.67°E 19.08°N	124.54°–124.88°E 19.05°–19.20°N	September 9, 2019	49	NOTC	TJU ^c

^aOcean University of China. ^bQingdao HiSun Ocean Equipment Co., Ltd. ^cTianjin University.

thousands of Argo floats in conjunction with satellite observations (Zhao et al., 2016). Hennon et al. (2019) estimated the temperature signals derived from the Argo floats that are imparted by internal tides and showed that there is a small, positive correlation between the stationary internal tides derived from altimetry and in situ signals, providing a practical way that links local temperature fluctuations with internal tides. Specifically, the relationship is more prominent in regions full of intense internal waves, as well as at depths near the nominal mode-1 maxima.

As the most widely known internal waves in the ocean, internal tides are commonly generated by barotropic tides flowing over rough topography and provide mechanical energy for deep ocean mixing (Ferrari & Wunsch, 2009; Garrett & Kunze, 2007). Furthermore, global deep ocean mixing is thought to be dominated by internal tides which contribute half of the energy to sustain the deep ocean stratification and maintain the meridional overturning circulation (Munk & Wunsch, 1998). However, in spite of the well-known global distribution of internal tide generation, its propagation and dissipation are not well understood, especially in the deep ocean (Vic et al., 2019). Compared with the upper 2,000 m of the ocean, observational studies of internal tides in deep oceans are quite limited due to insufficient in situ data (Levin et al., 2019).

To increase the sampling density below 2,000 m, full-depth floats were designed with the aim of having 1,200 floats in the future global ocean (Johnson et al., 2015; Kobayashi et al., 2011; Le Reste et al., 2016; Roemmich, Alford, et al., 2019; Roemmich, Sherman, et al., 2019). The original purpose of maintaining over 1,000 Deep Argo floats is to close the heat, freshwater, and sea-level budgets, characterize decadal variability in deep ocean water masses and estimate the mean and decadal variability in deep ocean circulation including the meridional overturning circulations (Johnson et al., 2015). Because of the nearly 250 Deep Argo floats deployed in deep areas of the South Pacific, South Indian, and Atlantic Ocean, we are currently able to estimate the warming rate of deep water in some basins (Johnson et al., 2019, 2020) and reexamine the deep currents in some basins (Racapé et al., 2019; Tamsitt et al., 2019; Zilberman et al., 2020). Likewise, it is possible to have assessments on internal

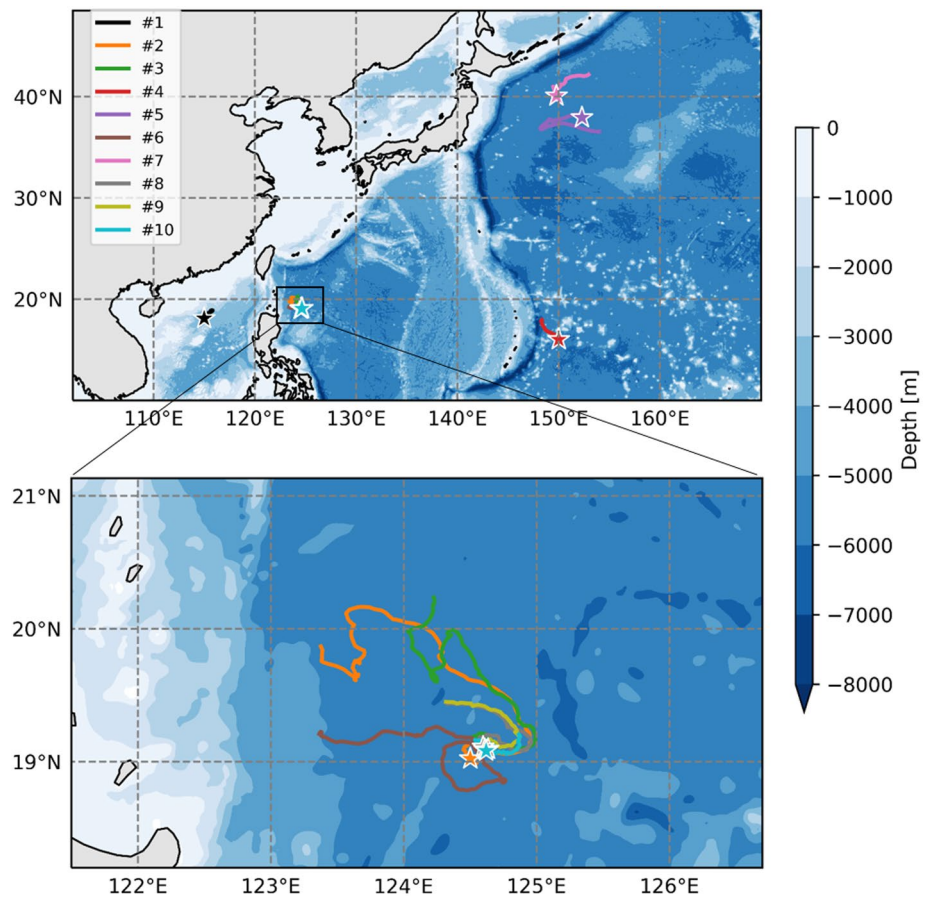


Figure 1. Deployment locations and trajectories of 10 deep profiling floats.

waves in deep oceans and their impacts on changes of local water properties when Deep Argo arrays become more available as deep ocean observational data are continuously accumulating.

Quantifications of fluctuations in temperature induced by deep ocean internal waves are challenging, but of great importance is trying to provide a range of uncertainties when one attempts to estimate deep ocean warming rate by sporadic Deep Argo floats. It is possible that, at a certain depth, high-frequency temperature fluctuations may alias on the profiles obtained by Deep Argo floats, which introduce uncertainties in evaluating the deep ocean warming rate (Johnson et al., 2019). In this regard, it is necessary to first tell how much fluctuations of temperature that internal waves account for before we can confidently evaluate the warming/cooling trend using the increasing numbers of Deep Argo floats.

In this study, we analyzed five daily sampling deep profiling floats deployed in the South China Sea (SCS) and Western Pacific (WP), and attempted to assess the temperature fluctuations induced by internal waves. Results show that the internal waves, either internal tides or near-inertial waves, have considerable imprints on deep ocean temperature fluctuations and may potentially give rise to spurious signals when assessing the deep ocean warming rate via sporadic Deep Argo floats. Given the incomplete knowledge on deep ocean internal tides with respect to their geographical distributions of energy conversion, evolution, fate, and parameterization scheme, the results in this study may provide some favorable references. The rest of this paper is organized as follows: in Section 2, we introduce the deep profiling floats deployed in 2019, as well as the data and procedure used to extract internal

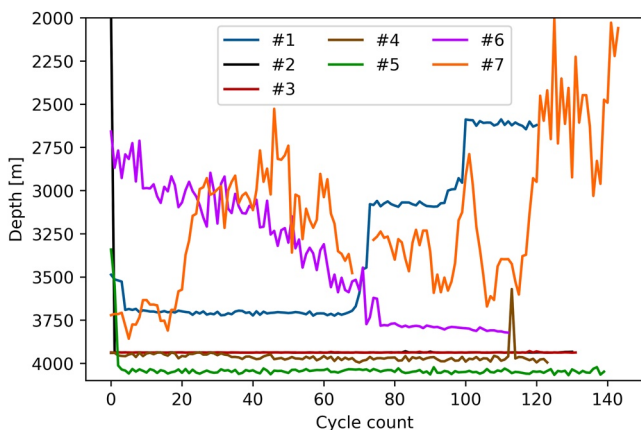


Figure 2. The maximum depth of deep profiling floats.

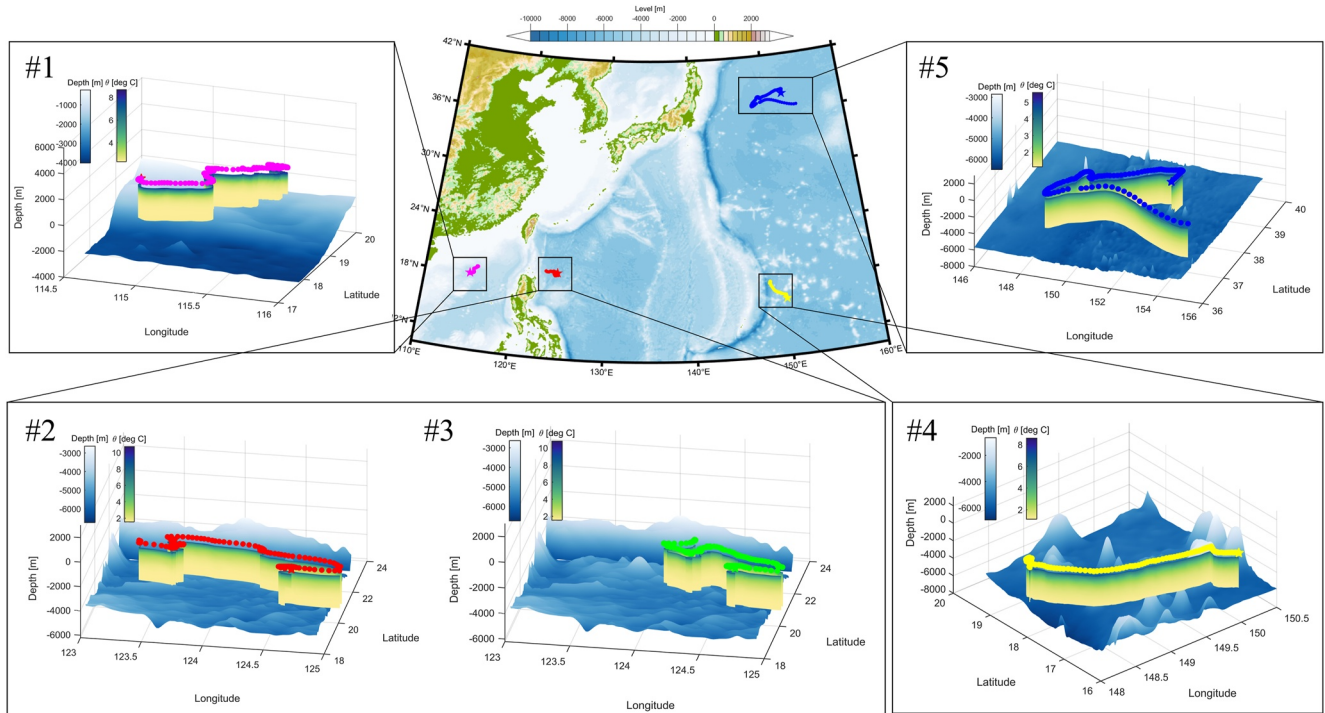


Figure 3. Temperature profiles of five deep profiling floats in the South China Sea (SCS, #1), Philippine Basin (PB, #2 and #3), Mariana Arc (MA, #4), and Kuroshio Extension (KE, #5), with topography being overlaid.

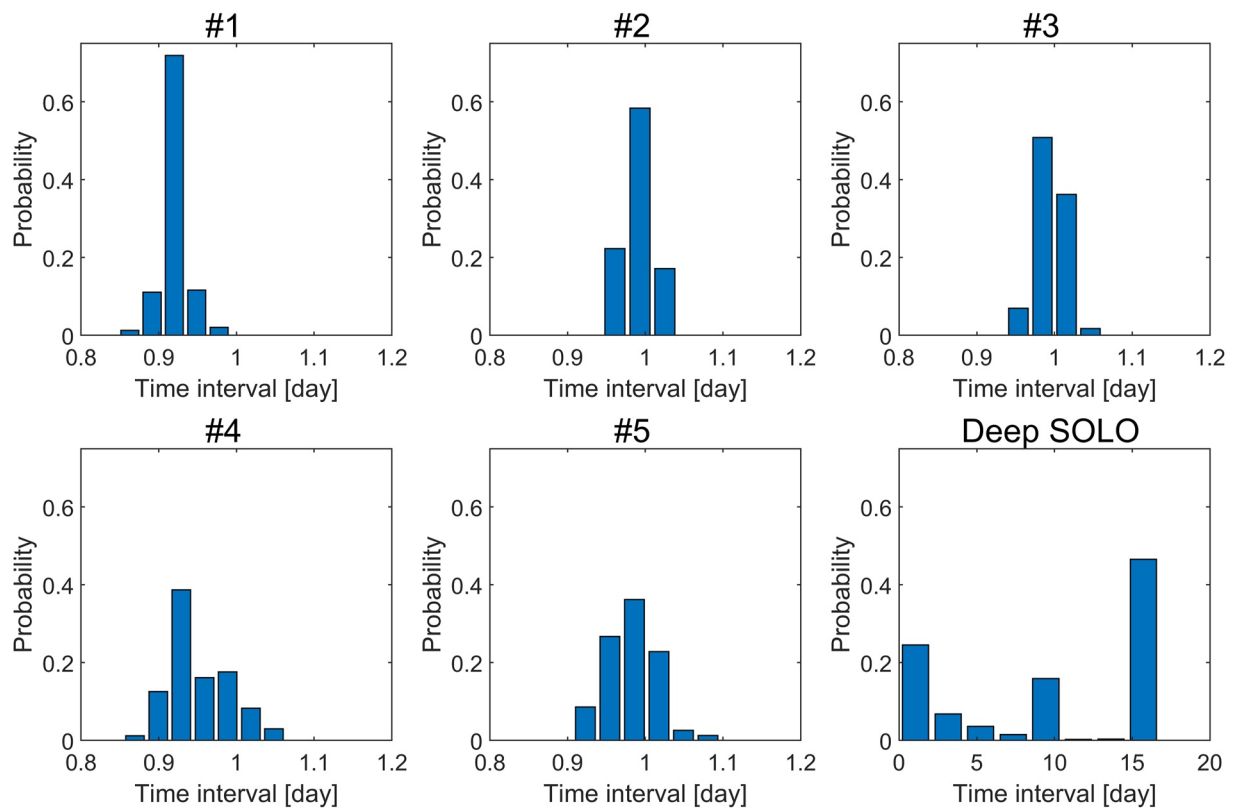


Figure 4. The probability density function (PDF) of time intervals between adjacent profiles for the selected deep profiling floats and Deep SOLOs.

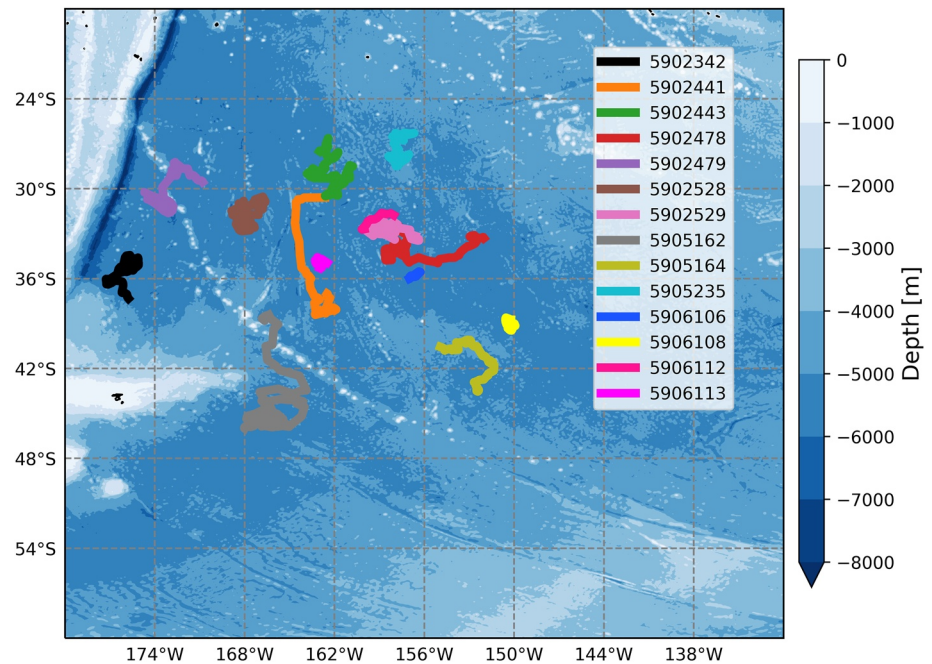


Figure 5. Trajectories of 14 Deep SOLO floats in the Southwest Pacific. The IDs of Deep SOLO floats are indicated.

wave imprints on temperature. Detailed results, including the temperature fluctuations at the tidal and inertial frequencies, will be presented in Section 3. The feasibility of sampling strategies was verified by comparing with nearby moorings in Section 4, followed by the summary and discussion of this study in Section 5.

2. Data and Methods

2.1. Deep Profiling Floats and Deployment in 2019

China began the development of 4,000-m profiling floats in 2016 (Deep Argo Workshop second report, 2019). In 2019, 10 prototypes of 4,000-m deep profiling floats designed and manufactured by Ocean University of China, Qingdao HiSun Ocean Equipment Co., Ltd. and Tianjin University (Table 1) were deployed in the SCS, Philippine Basin (PB), Mariana Arc (MA), and Kuroshio Extension (KE) (Figure 1). All three models of deep profiling float were designed technically following the Deep SOLO floats (Roemmich, Sherman, et al., 2019), and adopted a glass ball with the controller and lithium batteries inside; hydraulic system, satellite transmission module and related sensors outside. The whole system is about 55 kg and expected to work normally under pressure of up to 50 Mpa (~5,000 m).

It should be noted that nine prototypes were equipped with a SBE-37sm CTD rather than the conventionally used SBE-41/41CP/61 CTDs manufactured by Sea-Bird Electronics. Being not a specialized CTD designated for mobile platforms, the SBE37sm CTD equipped on a profiling float does not perform as well as conventional CTD, particularly for the conductivity/salinity data. Since we only focus on ocean temperature measured by the profiling float, as will be discussed later, it will not pose too serious a problem on the data analysis or change our conclusions substantially.

To verify the stability and working performance of the floats in a short time as much as possible, all the deep profiling floats were set a daily repeated cycling with the maximum profiling depth down to 4,000 m. Different from the 1,000 m parking depth of routinely used Deep Argo floats, no parking depth was set for the testing floats, which means all floats sample up and down all the time. There were six floats, including one OUC, one TJU, and four HM4000, deployed in the PB, and the other four OUC floats were deployed in the SCS, MA, and KE regions, respectively (Figure 1 and Table 1).

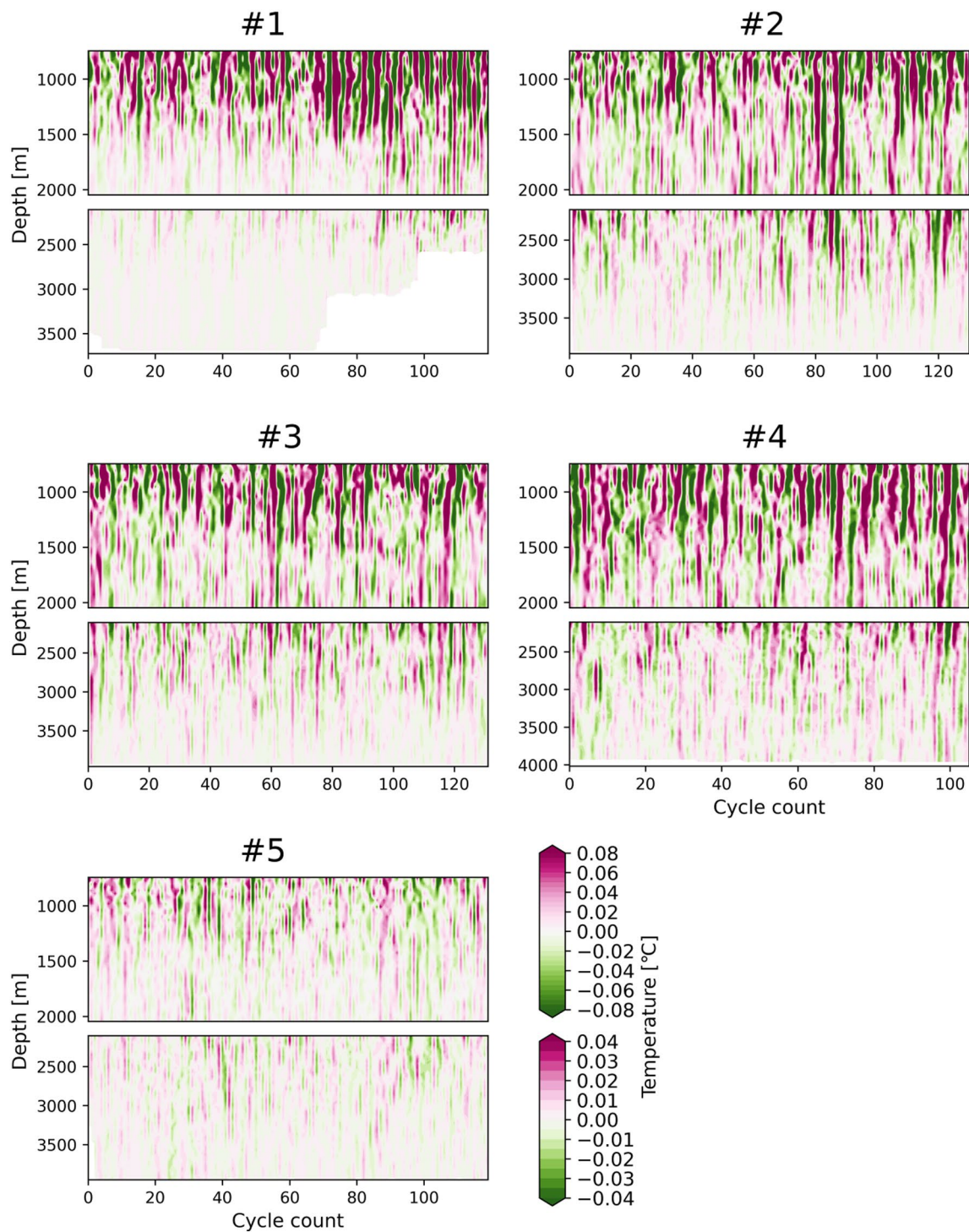


Figure 6. Profile-to-profile variability of temperature. Two color-bars are labeled for the results above/below 2,000 m.

2.2. Performance of Deep Profiling Floats

In terms of the total number of profiles, there are seven floats (#1, #2, #3, #4, #5, #6, and #7) that reached over 100 cycles and 3 floats (#8, #9, #10) only reached ~50 cycles (Table 1). Considering at least 65 cycles needed for harmonic analysis, as will be stated in Section 2.3, floats #8, #9, and #10 are excluded in the subsequent analysis.

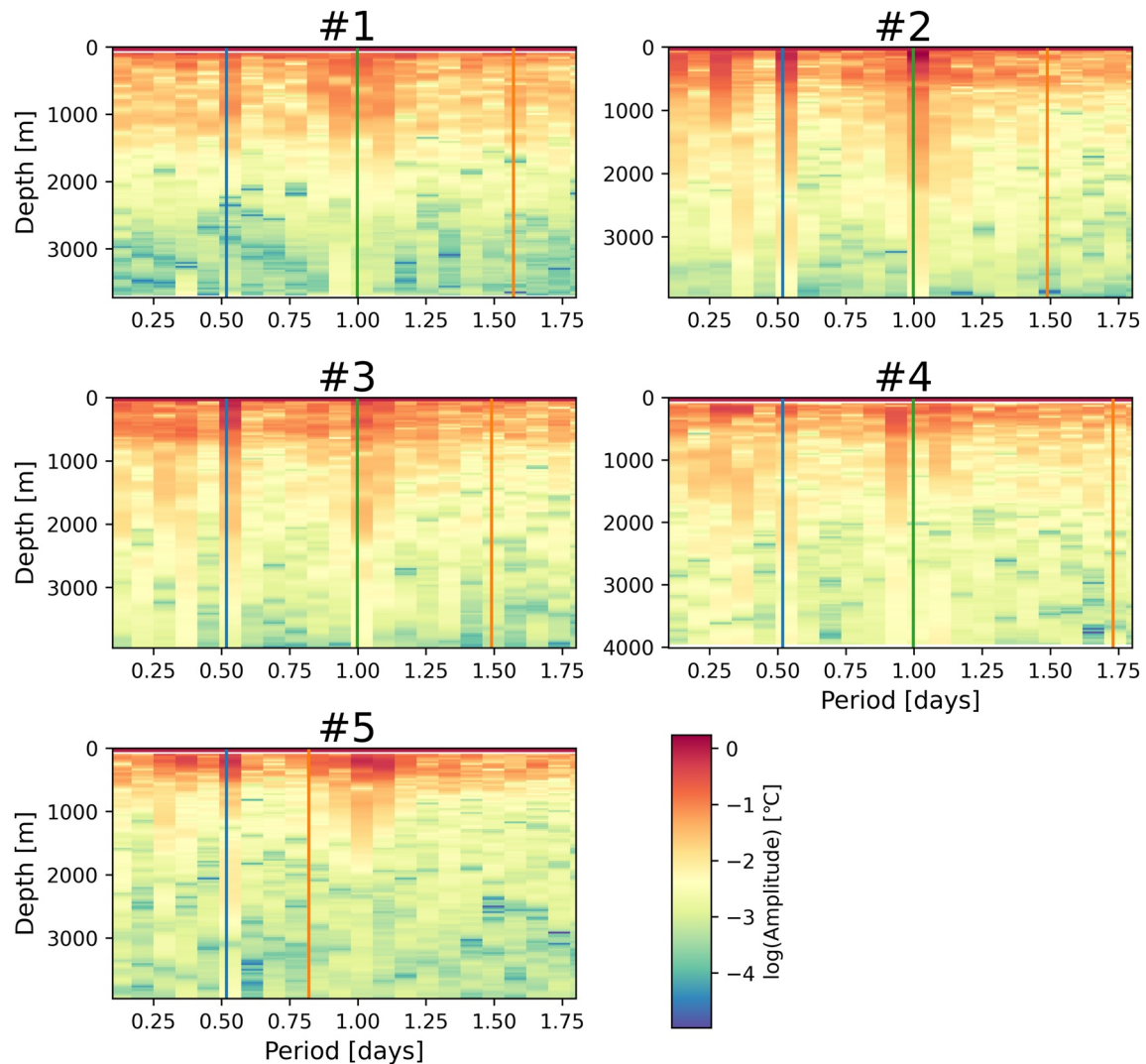


Figure 7. Amplitude of temperature fluctuations (logarithmic scale) derived from floats #1, #2, #3, #4, and #5 within the period band 0.1–1.8 days. The blue line, green line, and orange line denote semidiurnal, diurnal, and near-inertial frequency, respectively.

Among these prequalified floats, the maximum depth of #6 and #7 was quite unstable (Figure 2), indicative of a bad performance on buoyancy control. Thus, floats #6 and #7 were excluded in the following analysis. The maximum diving depth of float #1, though shallower than 4,000 m and behaved somewhat unstable during its lifetime, it was not excluded because the maximum profiling depth was adjusted concurrently according to its trajectory and local topography in the northern part of SCS. In this study, therefore, we only use five deep profiling floats (#1, #2, #3, #4, and #5) that were qualified in their performance on stable profiling maximum depth and sufficient repeated cycles.

Figure 3 shows the temperature profiles of the five selected deep profiling floats in the WP and SCS. For float #1, it drifted northeastward before reaching the continental slope region of SCS, with a distance of approximately 100 km during its lifetime. For floats #2 and #3, they both shifted northwestward over 100 km away from their deployment locations. Float #4 was deployed near MA and its trajectory appeared to be drifting northwestward due to the background North Equatorial Current (NEC). Float #5 was deployed within a warm-core eddy at the very beginning (figure not shown), and it drifted rapidly to the east after separating from the eddy and joined the swift eastward KE jet.

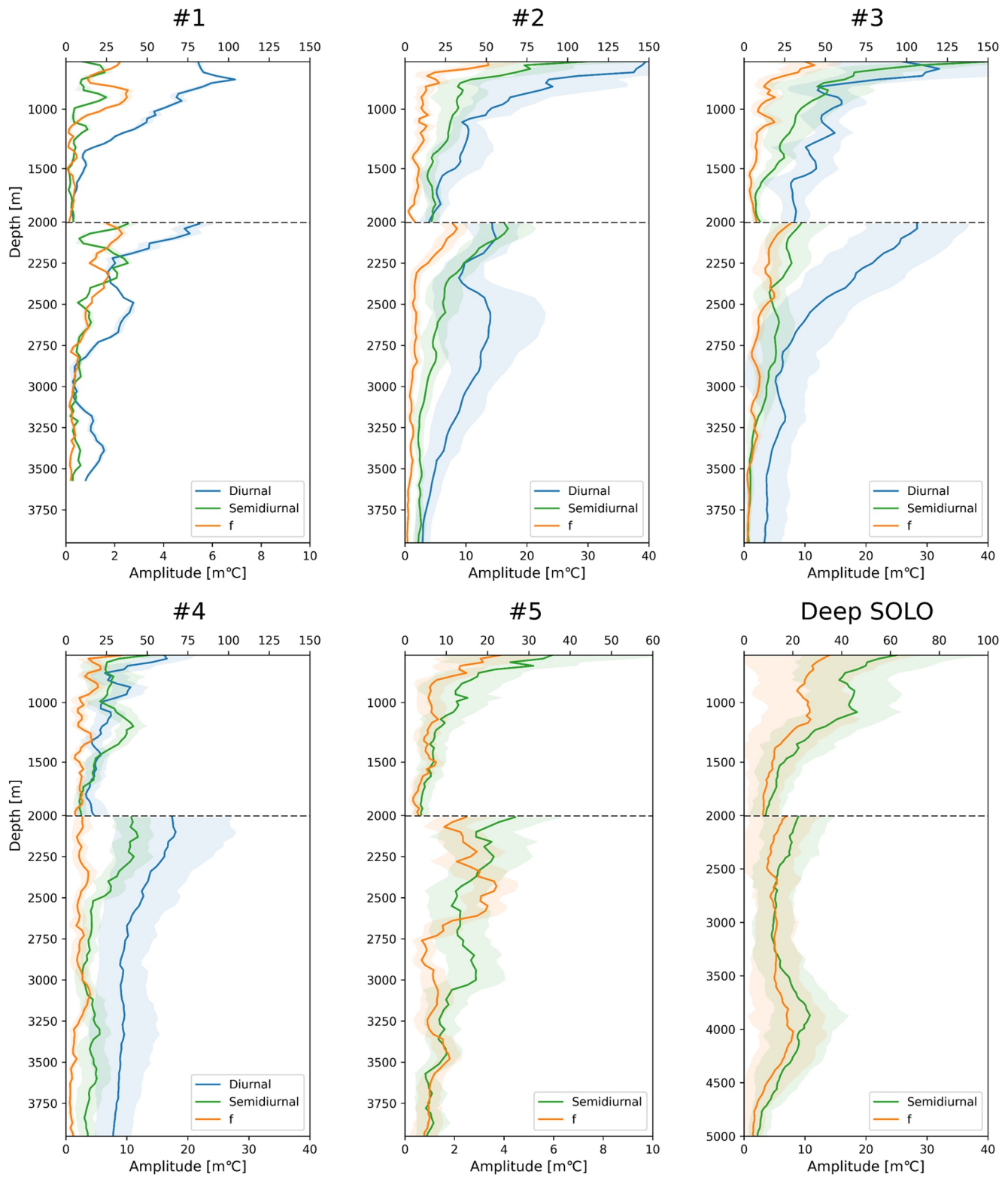


Figure 8. The temperature fluctuating amplitude induced by internal waves derived from five deep profiling floats and Deep SOLO floats. The blue, green, and orange lines denote the temperature amplitude at diurnal, semidiurnal, and near-inertial frequency, respectively. *Note.* Two different horizontal axes are labeled for the results above/below 2,000 m. The standard deviations are shown in shaded. Here, for Deep SOLO floats, the standard deviation is calculated from the amplitudes of all 14 floats.

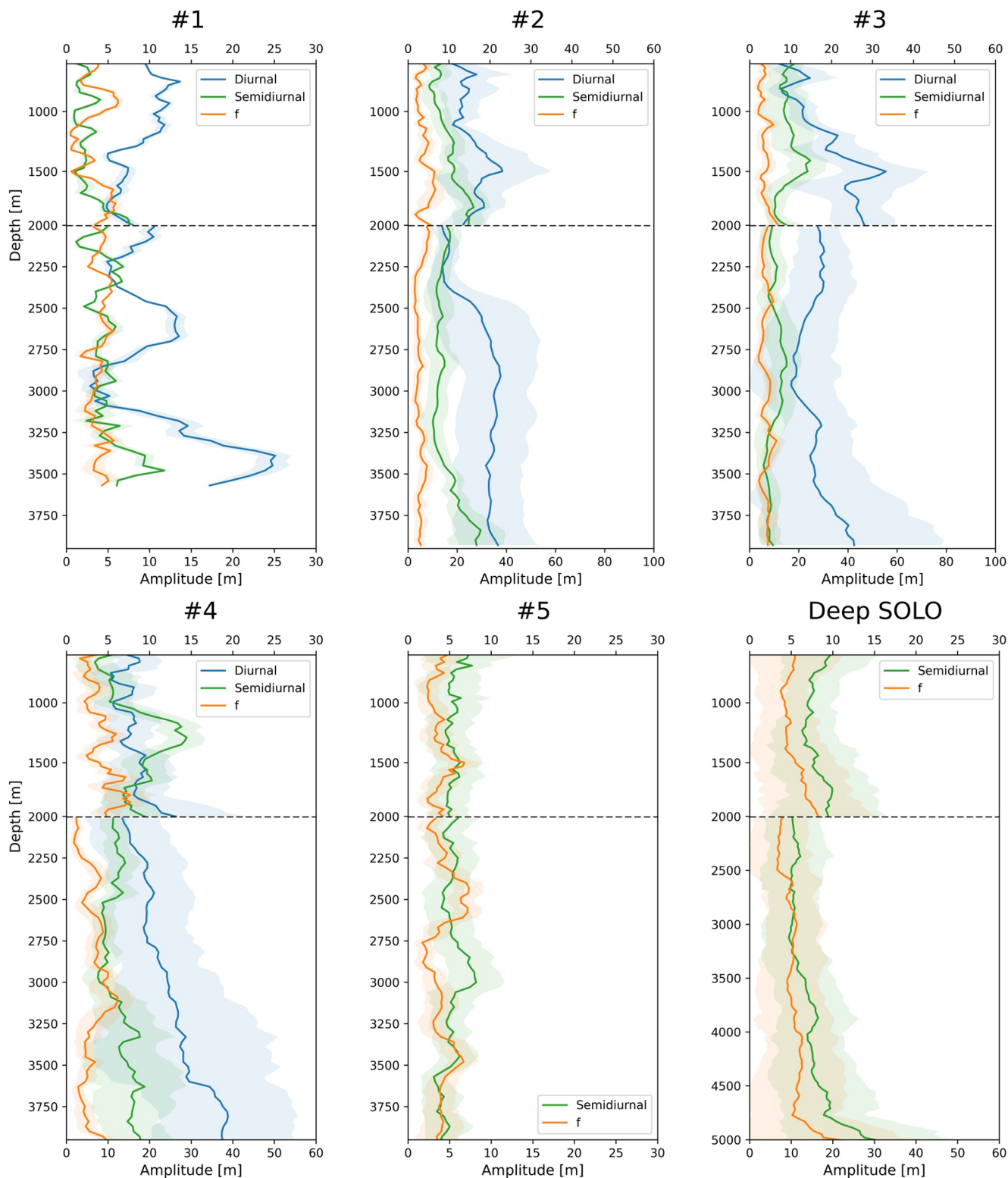


Figure 9. As in Figure 8, but for the vertical displacement.

Table 2
Temperature Amplitude ($m^{\circ}C$) and Its Standard Deviation at 3,000 m

Frequency	SCS		PB		MA	KE	SP
	#1	#2	#3	#4	#5	Deep SOLOs	
Diurnal	0.32 ± 0.15	10.72 ± 3.97	5.28 ± 5.12	9.28 ± 4.12	—	—	
Semidiurnal	0.36 ± 0.09	3.62 ± 1.17	3.80 ± 1.65	2.73 ± 1.34	2.86 ± 1.18	4.87 ± 3.43	
Near-inertial	0.34 ± 0.06	1.10 ± 0.58	2.51 ± 0.68	2.71 ± 0.78	1.14 ± 0.52	5.36 ± 4.93	
Total	1.02 ± 0.21	15.44 ± 3.53	11.59 ± 5.27	14.73 ± 4.58	4.00 ± 1.36	10.22 ± 5.95	

Although the deep profiling floats were set to dive and rise once a day, the cycling period is not as accurate 24 hr as expected. The sampling time intervals were influenced by a variety of factors such as the maximum profiling depth, background currents, density contrast between adjacent profiles, time spent during data communications, etc. Generally, as shown in Figure 4, the selected five deep profiling floats profiled once a day following prescribed configurations, particularly for floats #2, #3, and #5. Float #1 profiled somewhat faster at an average time interval of 22 hr, which is presumably due to insufficient profiling range in the shallower part of the northern SCS.

2.3. Extracting Temperature Fluctuations and Isopycnal Displacement Induced by Internal Waves

To quantitatively evaluate how much deep ocean temperature fluctuations are contributed by internal waves, particularly for internal tides and near-inertial waves, we conducted a series of harmonic analysis on potential temperature at certain depths. This is a simple but effective approach to extract signals at different frequencies. It should be noted that the selected five deep profiling floats adopted two sampling strategies. For floats #1, #4, and #5 (OUC model), the sampling interval was set 5 min, while floats #2 and #3 (HM4000 model) ascend and sample at preprogrammed layers. In this sense, all temperature data were interpolated onto the pressure grid from surface to the maximum depth with a vertical interval of 30 dbar.

Assume the time series of potential temperature at a certain pressure level z can be represented as a linear combination of a set of sinusoidal terms:

$$T(z, t) = T_0(z) + \sum_{j=SD, D, f, x} (H_j(z) \cos(\sigma_j t - g_j(z))) \quad (1)$$

where $T(z, t)$ is the measured temperature time series, $T_0(z)$ is the mean value, $H_j(z)$ and $g_j(z)$ are the amplitude and phase of cosine wave package at frequency σ_j . Here, $M_2(1/12.4206 \text{ hr}^{-1})$ and $K_1(1/23.9345 \text{ hr}^{-1})$ are selected representative of main semidiurnal (SD) and diurnal (D) constituents, and f denotes the local inertial frequency. In addition to the selected frequency bands, we linearly discretize the pending period x from 0.1 to 1.8 days with an interval of 0.08 days.

Now, Equation 1 can be converted linearly into a set of parameters a_j and b_j and rewritten as:

$$T(z, t) = T_0(z) + \sum_{j=SD, D, f, x} (a_j(z) \cos(\sigma_j t) + b_j(z) \sin(\sigma_j t)) \quad (2)$$

where

$$H_j(z) = \sqrt{a_j^2(z) + b_j^2(z)}, \quad g_j(z) = \arctan(b_j(z)/a_j(z)) \quad (3)$$

In this regard, amplitude and phase at each frequency can be obtained according to the input time series of potential temperature.

Note that the above harmonic analysis only works in the condition of a fixed location where stationary internal tidal signals are assumed constant. However, some of the deep profiling floats drifted over 100 km. The long-distance drifting is comparable to the typical wavelength of low-mode internal tides, which propagate over nearly a thousand kilometers from their generation. The amplitude and phase extracted from the original time series may be contaminated by introducing signals from spatial distribution of internal tides. In this case, to minimize the poten-

Table 3
As in Table 2, but for the Vertical Displacement (m)

Frequency	SCS		PB			MA	KE	SP
	#1	#2	#3	#4	#5	Deep SOLOs		
Diurnal	3.30 ± 1.60	29.60 ± 13.18	17.58 ± 17.03	24.29 ± 12.46	—	—		
Semidiurnal	3.69 ± 0.84	12.05 ± 3.88	12.63 ± 5.46	12.46 ± 3.91	8.11 ± 1.18	10.25 ± 7.22		
Near-inertial	3.51 ± 0.53	3.65 ± 1.93	8.33 ± 2.54	9.33 ± 2.87	3.23 ± 1.49	11.28 ± 10.37		
Total	10.50 ± 2.11	51.33 ± 11.68	38.54 ± 17.54	41.43 ± 15.87	11.34 ± 3.84	21.53 ± 12.54		

tial influence from these signals, we apply a 65-point (nearly 65-day) moving window for the subsequent harmonic analysis (sensitivity experiment for the moving window can be seen in Part 4). Similar to the above equations, we only extract the semidiurnal, diurnal, and inertial components from the original temperature time series as:

$$T(z, t) = T_0(z) + \sum_{j=SD, D, I} (H_j(z) \cos(\sigma_j t - g_j(z))) \quad (4)$$

Equation 4 can be converted linearly into a set of parameters a_j and b_j and rewritten as:

$$T(z, t) = T_0(z) + \sum_{j=SD, D, I} (a_j(z) \cos(\sigma_j t) + b_j(z) \sin(\sigma_j t)) \quad (5)$$

Following Huang et al. (2018), the vertical displacement amplitude $A_j(z)$, can be calculated through $H_j(z)/T_z(z)$. Here, $H_j(z)$ denotes temperature amplitude calculated from the above equations, and $T_z(z)$ denotes the vertical gradient of background potential temperature calculated from averaged temperature profile. Note that the harmonic analysis with 65-point harmonic window obtained a series of amplitudes and its standard deviation was calculated subsequently.

2.4. Modal Decomposition and Energy for Internal Tides

The baroclinic modes for vertical displacement, $\Phi(z)$, can be determined by the Sturm-Liouville equation,

$$\frac{d^2 \Phi(z)}{dz^2} + \frac{N^2(z)}{c_n^2} \Phi(z) = 0 \quad (6)$$

subject to the boundary conditions $\Phi(0) = \Phi(-H) = 0$, where n is the mode number and c_n is the eigenspeed (Gill, 1982). The $N^2(z)$ is the averaged squared buoyancy frequency.

The vertical displacement is expressed as:

$$\eta'_j(z, t) = \sum_{n=1}^5 \eta'_n(t) \Phi_n(z), \quad (7)$$

where $\Phi_n(z)$ is the vertical structures, $\eta'_n(t)$ represent the time-varying magnitude of the n th mode and $\eta'_j(z, t)$ denotes the reconstructed time-varying vertical displacement. In this study, we used the first five modes to extract

Table 4
Temperature Amplitude (m °C) and Its Standard Deviation Near the Depth of 4,000 m

Frequency	SCS (3,570 m)		PB (3,930 m)		MA (3,930 m)	KE (3,930 m)	SP (3,990 m)
	#1	#2	#3	#4	#5	Deep SOLOs	
Diurnal	0.99 ± 0.11	2.94 ± 1.28	3.46 ± 5.44	7.83 ± 3.00	—	—	
Semidiurnal	0.34 ± 0.07	2.26 ± 0.93	0.71 ± 0.85	3.46 ± 1.43	0.88 ± 0.43	9.87 ± 5.57	
Near-inertial	0.23 ± 0.07	0.39 ± 0.17	0.61 ± 0.32	0.94 ± 0.45	0.87 ± 0.69	7.23 ± 5.71	
Total	1.59 ± 0.16	5.59 ± 1.96	4.78 ± 3.14	12.23 ± 4.31	1.75 ± 1.00	17.10 ± 9.33	

Table 5
As in Table 4, but for the Vertical Displacement (m)

Frequency	SCS (3,570 m)	PB (3,930 m)		MA (3,930 m)	KE (3,930 m)	SP (3,990 m)
	#1	#2	#3	#4	#5	Deep SOLOs
Diurnal	20.96 ± 2.01	36.04 ± 15.74	42.40 ± 36.02	37.37 ± 16.81	—	—
Semidiurnal	7.25 ± 1.31	27.67 ± 11.39	8.76 ± 4.36	16.81 ± 7.53	4.11 ± 0.43	14.98 ± 8.45
Near-inertial	4.89 ± 1.45	4.81 ± 2.12	7.49 ± 3.16	7.18 ± 2.70	4.07 ± 3.24	10.97 ± 8.68
Total	33.51 ± 2.77	68.53 ± 24.13	58.64 ± 38.40	61.42 ± 23.56	8.18 ± 4.75	25.95 ± 14.16

the vertical displacement of baroclinic mode. Although the phase of vertical displacements was considered here, the vertical structure for each mode may be aliased due to the nearly 1-day sampling strategies.

The depth-integrated available potential energy (APE) for n th baroclinic mode is calculated through

$$APE = \frac{1}{2} \rho_0 \int_{-H}^0 \langle N^2(z) \eta_n^2(z, t) \rangle dz. \quad (8)$$

Here, ρ_0 denotes the water density, H denotes the water depth, and the angle brackets denote an average over one semidiurnal and diurnal tidal period. The $\eta_n(z, t)$ denotes the time-varying vertical displacement of the n th mode.

2.5. Mooring Data and Other Deep Argo Floats Data

To demonstrate and validate the approach we used to analyze the temperature data measured by deep profiling floats, we used the CTD data from three subsurface moorings nearby, which are located at SCS and PB, respectively. In the SCS, the subsurface mooring was deployed at the northern part of SCS (18.33°N, 115.93°W) on

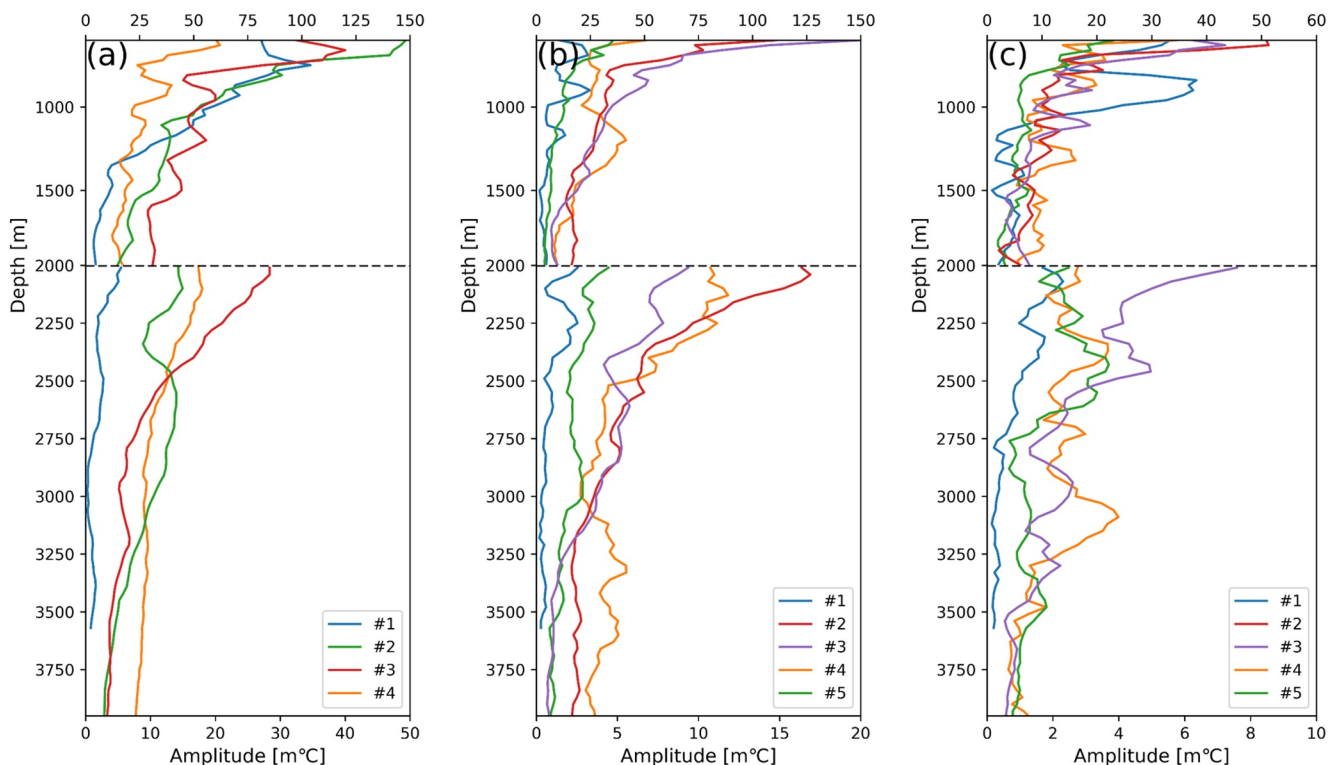


Figure 10. The mean temperature fluctuating amplitudes derived from five deep profiling floats at (a) diurnal, (b) semidiurnal, and (c) near-inertial frequencies. *Note.* Two different horizontal axes are labeled for the results above/below 2,000 m.

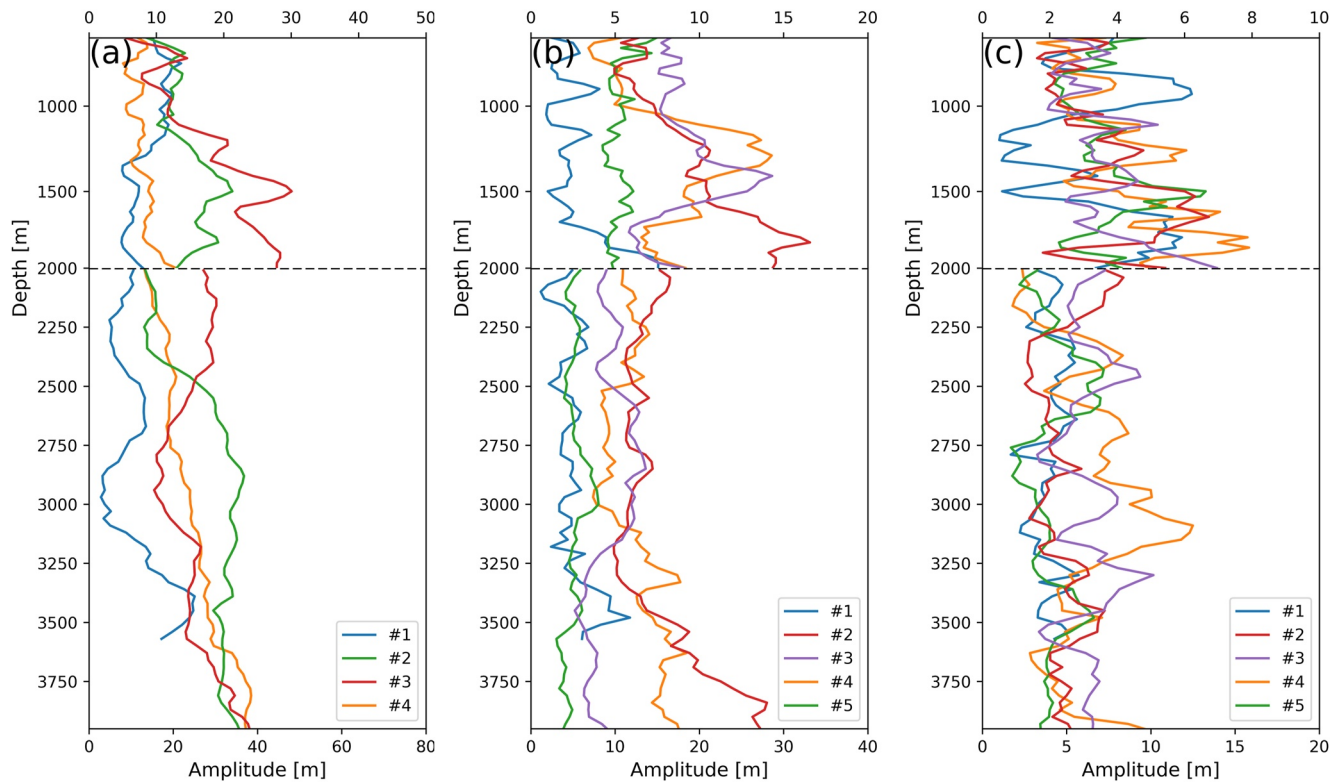


Figure 11. As in Figure 10, but for the vertical displacement.

August 31, 2017 and recovered on August 19, 2018 (Figure 13a). It collected temperature/salinity/pressure data every 30 min. The other two moorings were deployed at PB (Figure 13b): mooring #1 (20°N, 127°W) was started on October 16, 2019 and recovered on 14 September 2020 and mooring #2 (19°N, 128.5°W) was started on October 16, 2019 and recovered on September 13, 2020. The two moorings in the PB collected temperature/salinity/pressure data every 10 min. The results derived from the subsurface moorings, as will be discussed in Section 4, are consistent with those from the deep profiling floats.

To test the feasibility of harmonic analysis in extracting the target signals with a lower sampling frequency (e.g., 10 days per cycle), we conducted the same analysis on the temperature recorded by recently deployed Deep SOLO floats. Deep SOLO is a full-depth profiling float for the Deep Argo array, which collects temperature and salinity profiles from the surface to 6,000 m every 10 days (Roemmich, Sherman, et al., 2019). In this study, we chose 14 floats deployed in the deep basin of the South Pacific (SP) because these floats have sufficient profiles down to 5,000 m (Figure 5). According to Roemmich, Sherman, et al. (2019), the vertical speed of Deep SOLO is about 0.13 m/s so that the sampling time can be roughly estimated by two adjacent profiles. Similarly, we linearly interpolated the temperature data and the corresponding sampling time onto a uniform vertical grid of 30-dbar interval.

3. Results

3.1. Profile-to-Profile Variability of Temperature

Before performing harmonic analysis, it is beneficial to first check the profile-to-profile variability as seen from the deep profiling floats. For simplicity, we subtracted the measured temperature of adjacent profiles. It is shown in Figure 6 that, although the sampling period is not exactly one day, prominent alternation of temperature between sequential profiles can still be found, indicative of the potential impact of internal tides on local isopycnal displacement. In particular, the profile-to-profile variability is more evident in upper 2,000 m. Below 2,000 m, the temperature fluctuations become weaker. For those deep profiling floats (#2, #3, and #4) deployed in the

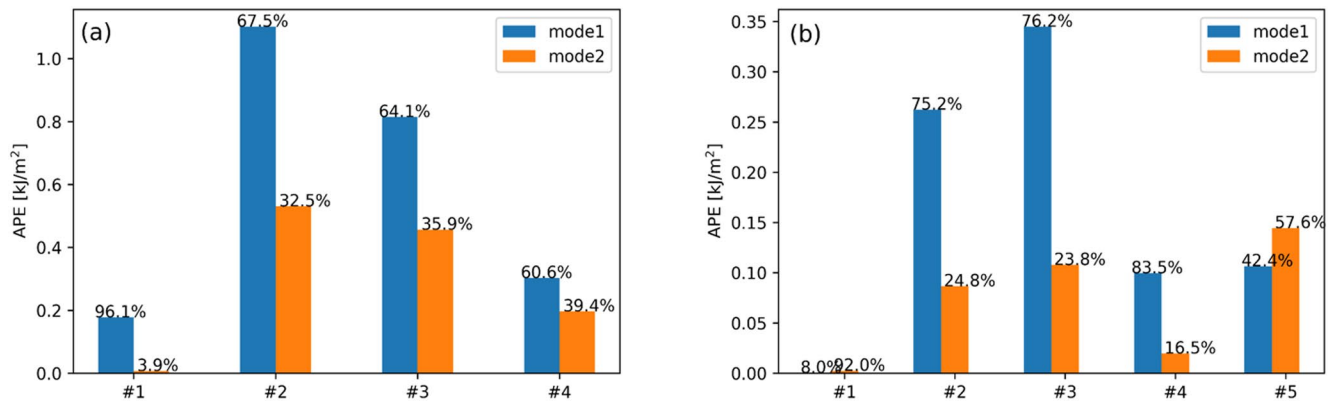


Figure 12. The mode-1 and mode-2 available potential energy (APE) of (a) diurnal and (b) semidiurnal internal tides for floats #1, #2, #3, #4, and #5.

PB and MA region, the temperature fluctuations appear to be more remarkable. For float #1, the temperature variability becomes more significant with its trajectory approaching to the continental shelf, implying enhanced internal waves generations on steep slopes (Xu, Liu, et al., 2016).

3.2. Temperature Fluctuations and Isopycnal Displacement Induced by Internal Waves

According to Equation 2, the amplitude of temperature at each frequency can be derived using harmonic analysis. Figure 7 demonstrates the calculated temperature fluctuations as functions of depth. Note that despite the amplitudes of temperature decrease with increasing depth, a striking feature in Figure 7 is there exhibits large values of temperature amplitude at certain frequency bands, particularly at tidal frequencies such as semidiurnal and diurnal frequencies. With respect to the near-inertial band, however, it is difficult to be well distinguished in most cases. Next, we only conduct specific harmonic analysis following Equations 4 and 5 regarding the internal tides and near-inertial waves to highlight their contributions to the temperature fluctuations in different regions.

3.2.1. South China Sea

In the northern part of SCS, the diurnal signal is much more prominent between 600 and 1,600 m (results of upper 600 m are all excluded in the following figures), indicative of strong internal tides at diurnal frequency in this region (Alford et al., 2015; Jan et al., 2007; Klymak et al., 2011; Zhao, 2014). In particular, the diurnal component can account for approximately 0.1 °C in the upper 1,000 m (Figure 8, #1). Detailed examinations indicate that the amplitudes at three main frequencies decreased rapidly with increasing depth and the signals are somewhat weak below 2,600 m. In the deep layer greater than 3,000 m, the total fluctuating amplitude of temperature at three frequencies approaches about 1 m °C. However, The total vertical displacement of isopycnals at 3,500 m reaches over twice of that in the upper layer due to weak stratifications in the deep ocean (Figure 9 #1 and Tables 3 and 5), which requires less tidal shears to produce stronger diffusivities.

3.2.2. Philippine Basin

Floats #2 and #3 were deployed in the PB. The amplitudes of semidiurnal and diurnal signals are all prominent while the near-inertial component is relatively weak (Figure 7). As indicated previously, the configurations of two deep profiling floats deployed here are quite similar, so that the results derived from the two floats are consistent with each other. Generally, the amplitudes of signals at three frequency bands decrease with increasing depth, but the diurnal signals seem much more prominent than the semidiurnal and near-inertial signals (Figure 8).

However, detailed analysis shows that the total fluctuations reduce to less than half of that at 3,000 m for float #2 at the depth of 4,000 m, but the vertical displacement remains nearly unchanged (Tables 2 and 4 and Figure 9). For float #3, the vertical displacement increases to 58.64 ± 38.40 m (Table 5) at the depth of 4,000 m although the temperature fluctuations are stable below 3,000 m. The diurnal internal tide accounts for 5.59 ± 1.96 m °C for the local temperature fluctuations (Table 4). Compared to strong signals at diurnal frequency, the temperature fluctuating amplitude at semidiurnal and near-inertial frequencies are relatively weak, accounting for only 2.26 ± 0.93 m °C and 0.39 ± 0.17 m °C, respectively (Table 4). Here, it should be noted that the standard devi-

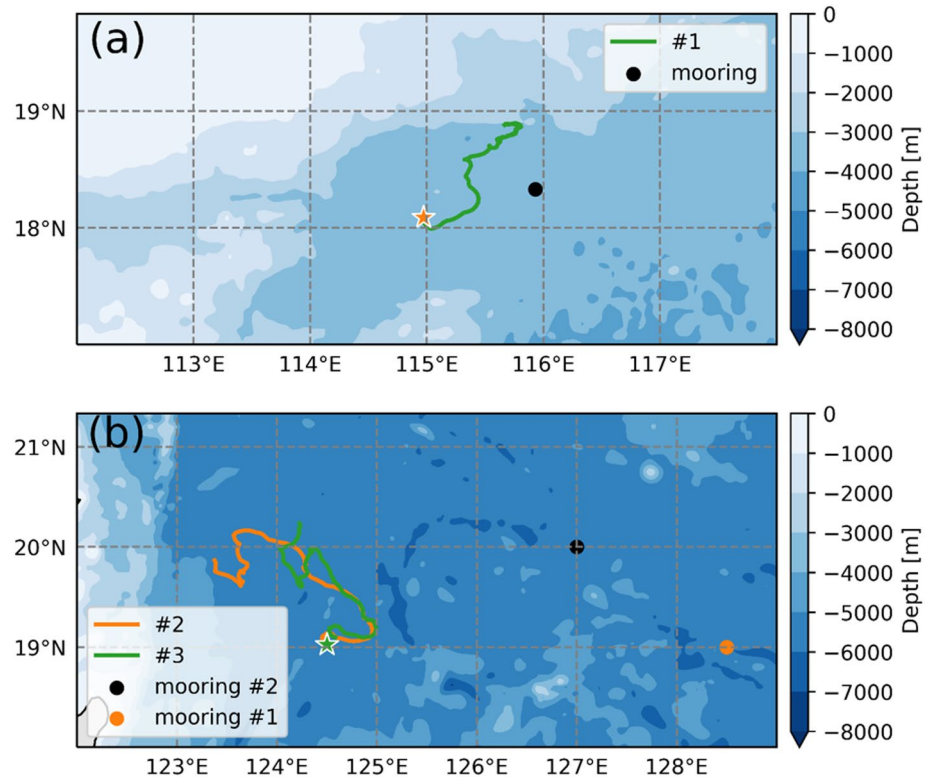


Figure 13. The trajectories of deep profiling floats and mooring location in the (a) South China Sea (SCS) and (b) Philippine Basin (PB).

ations are relatively large. These large standard deviations have resulted from the effects of seasonal changes of internal tides and variable pathways influenced by Kuroshio and mesoscale eddies (Alford et al., 2015; Huang et al., 2018; Xu et al., 2021).

3.2.3. Mariana Arc

In the MA region, the semidiurnal signals seem stronger than the diurnal one in the upper 2,000 m (Figure 8, #4). Unlike in other regions, the amplitudes of signals at three frequency bands do not vary too much especially in the deep ocean. Modal decomposition implies the existence of high mode internal tides (Figure 12, #4). In detail, the total temperature fluctuations reach up to 12.23 ± 4.31 m °C at 4,000 m, much larger than that in the PB (Table 4). Despite the uniform structure of temperature fluctuations below 3,000 m, the vertical displacement increases prominently below 2,000 m due to weak stratification in the deep ocean (Figure 9, #4). Specifically, the amplitude of vertical displacement reaches 61.42 ± 23.56 m °C at 4,000 m (Table 5). The significant vertical displacement reflects stronger internal tides generation in the MA and partly implies prominent turbulent diffusivity and mixing in the deep ocean there (Wang et al., 2018; Zhao & D'Asaro, 2011; Zhao et al., 2016, 2021).

3.2.4. Kuroshio Extension

In the KE region, the diurnal internal tides disappear (Figure 7, #5) and the amplitude of near-inertial signals are comparable with the semidiurnal one (Figure 8, #5) since the KE is a hot-spot for full of near-inertial waves (Liu et al., 2019; Rimac et al., 2013; Sun et al., 2021). In contrast to float #4, the temperature and vertical displacement amplitude of float #5 do not change substantially with increasing depth, which may be associated with the weak internal waves in the deep ocean over flat topography in this region.

3.3. Regional Difference of Internal Waves Imprints on Temperatures and Vertical Displacement

With respect to diurnal internal tides, it is shown in Figure 10a that the amplitude derived from float #1, which is deployed in the northern part of SCS, is comparable with all other floats in the upper 1,200 m, but it weakens

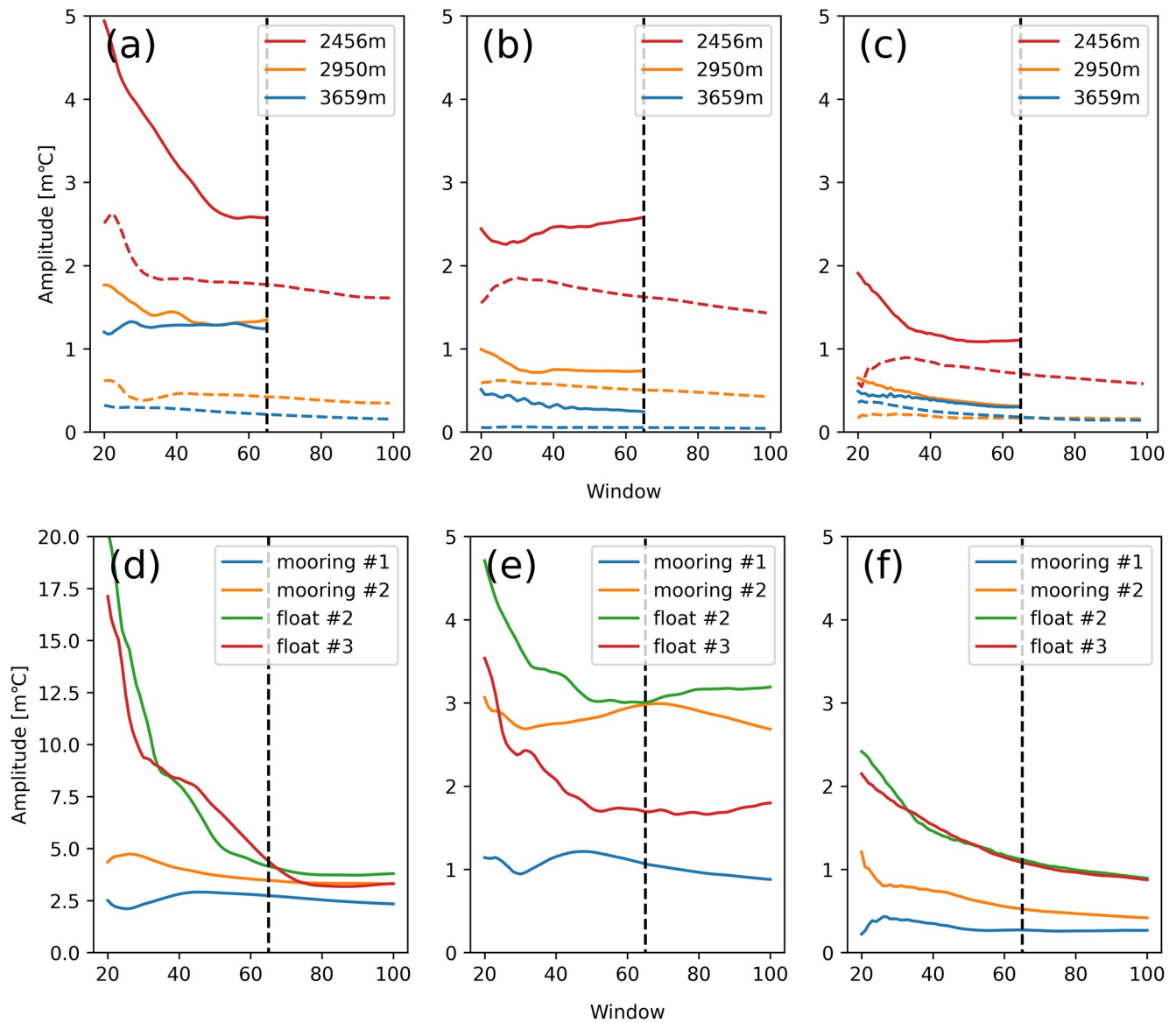


Figure 14. The amplitude of diurnal, semidiurnal, and near-inertial frequencies as a function of harmonic window in the (a–c) South China Sea (SCS) (dashed lines for deep profiling floats and solid line for mooring) and (d–f) Philippine Basin (PB). The black dotted lines denote the 65-point window.

rapidly below this depth. Instead, the temperature fluctuating amplitudes derived from floats #2, #3, and #4 are still large in the deep ocean, probably due to strong internal tides generated in these areas (Alford et al., 2011; Zhao, 2014; Zhao et al., 2016). The amplitudes are very close between floats #2 and #3, but more prominent for

Table 6
Temperature Amplitude (m °C) and the Standard Deviation at Three Levels Derived From the Subsurface Mooring and Float #1

Depth(m)	Diurnal		Semidiurnal		Near-inertial		Total	
	M	F	M	F	M	F	M	F
2,456	1.77 ± 0.33	2.57 ± 1.15	1.62 ± 0.20	2.58 ± 0.67	0.70 ± 0.21	1.10 ± 0.26	4.10 ± 0.48	6.25 ± 1.60
2,950	0.42 ± 0.14	1.35 ± 0.81	0.50 ± 0.08	0.73 ± 0.29	0.17 ± 0.06	0.31 ± 0.12	1.10 ± 0.18	2.39 ± 0.91
3,659	0.21 ± 0.07	1.24 ± 0.68	0.05 ± 0.01	0.24 ± 0.17	0.19 ± 0.10	0.21 ± 0.24	0.45 ± 0.16	1.79 ± 0.99

Note. M, Mooring; F, Float.

Table 7
Temperature Amplitude (m °C) and the Standard Deviation Derived From Subsurface Mooring (3,600 m) and Floats at PB

Frequency	Mooring #1	Mooring #2	Float #2	Float #3
Diurnal	2.73 ± 0.50	3.48 ± 0.69	4.15 ± 2.30	4.15 ± 2.30
Semidiurnal	1.06 ± 0.30	2.98 ± 0.29	3.00 ± 0.86	3.01 ± 0.86
Near-inertial	0.27 ± 0.13	0.53 ± 0.25	1.12 ± 0.56	1.12 ± 0.55
Total	4.07 ± 0.72	6.98 ± 0.71	8.28 ± 2.39	7.17 ± 3.42

float #4 whose maximum fluctuating amplitude could exceed 16 m °C even at the depth of 3,800 m (Table 4). In contrast to the temperature amplitude, the vertical displacement below 2,000 m generally increase but have different vertical structures (Figures 11a). Besides, the small proportion of mode-1 internal tides in APE partly implies higher tidal shears and mixing in the deep ocean, particularly in the MA region (Figure 12, #4, Wang et al., 2018). Compared to the diurnal frequency, the temperature fluctuating amplitudes at semidiurnal frequency derived from the five deep profiling floats are somewhat weaker, particularly for the deep ocean below 1,500 m (Figure 10b). The amplitude of temperature fluctuations from floats #2, #3, and #4 are more prominent than floats #1 and #2 (Figure 10b). Specifically, the amplitude derived from float #4 is much larger than the other four floats at 4,000 m, probably due to abundant generations of semidiurnal internal tides over rough topography near the MA (Zaron, 2019). Besides, the evidently increased vertical displacements of floats #2 and #4 below 3,000 m imply the role of tide-induced diapycnal diffusivity over rough topography (Figure 11b).

As for near-inertial waves, the amplitudes are found much weaker compared to the internal tides imprints on local temperature fluctuations, as shown in Figure 10c we applied the harmonic analysis with a 65-point (nearly 65 days) moving window to extract the near-inertial signals. However, the near-inertial waves are generally generated episodically by weather-scale events, for example, midlatitude storms and typhoons, while the results as seen from the floats are kind of 65-day average, which is likely to underestimate these episodically generated near-inertial waves.

3.4. Results From Deep SOLO Floats

In addition to rapid-sampling floats deployed in the WP, we employed 14 Deep SOLO floats currently operating in the SP to validate our preliminary results shown above. Here we use full-time series of temperature and salinity derived from Deep SOLO floats to extract internal wave signals. Likewise, we only derived the semidiurnal and near-inertial signals of temperature in this particular area where most of Deep SOLO floats are beyond the critical latitude of diurnal internal tides. Below 2,000 m, we find a relatively stable amplitude ranging from 3 to 10 m °C, with a local maximum at 3,800 m (Figure 8). Unlike the semidiurnal internal tides, the amplitudes at near-inertial frequency are generally weak, with the amplitude of 5.36 ± 4.93 m °C at the depth of 3,000 m (Table 2).

Despite large uncertainties among the floats, the results above are in good agreement with our findings by the deep profiling floats. Both of them indicate that a few millesimal degrees of temperate fluctuations are induced by internal waves either the tidal or near-inertial component. This has an important implication that internal waves play a nonnegligible role in assessing the long-term changes in deep ocean temperatures by deep profiling floats. In addition, the amplitude of vertical displacement increases prominently in the deep ocean, which implies nonnegligible diapycnal mixing and diffusivity in the deep layer, especially in the regions of rough topography.

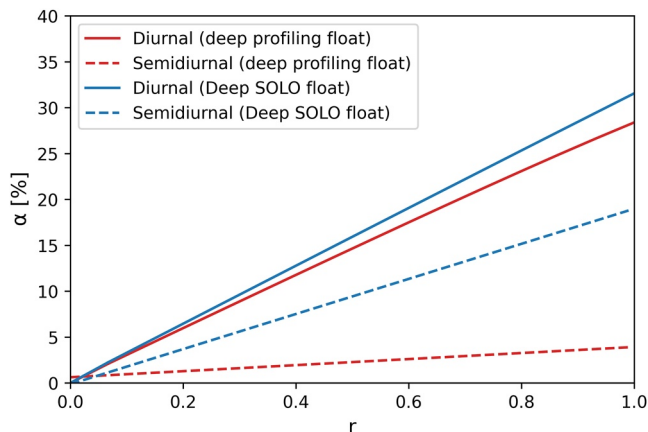


Figure 15. Relative error (α) as a function of r .

4. Discussions of Sampling Strategies

4.1. Role of the Harmonic Window

To determine a reasonable width of harmonic analysis window, we compared the results of the floats with nearby subsurface mooring (Figure 13). In general, the mooring results are more stable than the deep profiling floats because of high-frequency sampling (10 min or 30 min) and stable moored observation. Above the 65-point harmonic window, the amplitudes from all deep profiling floats are shown nearly stable (Figure 14). In detail, total differences of float #1 are ~ 2 m °C comparing with its nearby subsurface mooring at 2,456 m while ~ 1 m °C at 3,659 m (Table 6). In the PB, the total amplitude of mooring #2 is consistent with the floats (Table 7). The differences between moorings and deep profiling floats could be attributed to a variety

of reasons. First, the deep profiling floats are like a drifting platform and it is, therefore, a regional view of the averaging results. Second, the asynchronous observation time and locations for both moorings and deep profiling floats may cause unavoidable differences.

4.2. Role of Random Noise

The sampling frequency for the deep profiling floats is roughly 1 cpd, which is twice lower than the frequency of diurnal and semidiurnal internal tides. This sub-sampling time series may be contaminated more easily by unknown/random noises than high-frequency sampling. To quantify the uncertainties on our previous results, some ideal mathematical tests were conducted. Here we only investigated the diurnal and semidiurnal internal tides because near-inertial waves are much weaker.

We first generate an original signal, which consists of two sinusoidal signals with frequency of diurnal and semidiurnal. The amplitude of the original signal (A_{ori}) is 15 m °C and then superimposed by a series of white noises with amplitude ranging from 0 to 15 m °C. The ratio of white noise to original signal is defined as r , which ranges from 0 to 1. Following the same sampling strategy, we obtain the observed time series with sampling interval of 1 day analogous to deep profiling floats and 10 days analogous to Deep SOLO floats. Finally, the harmonic analysis is conducted to derive the amplitude of observed time series (A_{har}), with relative error being defined as $\alpha = \frac{A_{har} - A_{ori}}{A_{ori}}$.

It is shown in Figure 15 that α is linearly correlated with r , which means the harmonic analysis introduces more errors along with enhanced white noise both for the two sampling schemes. In particular, the relative errors increase nearly 30% if the amplitude of white noise is comparable to original signals. However, the noises in the real ocean are much less than observed signals, so that the uncertainties induced by random noises are acceptable, which do not change our conclusions substantially.

5. Summary and Discussion

In this study, we assessed the fluctuations in deep ocean temperature caused by internal waves in the South China Sea (SCS), Philippine Basin (PB), Mariana Arc (MA) and Kuroshio Extension (KE) using rapid-sampling (approximately 1 day) profiling floats down to 4,000 m. Results indicate that the internal waves, either internal tides or near-inertial waves have considerable imprints on local temperature changes. It is demonstrated that the internal tides appear much more prominent temperature fluctuations. Besides, the temperature fluctuations caused by internal waves at three frequencies are different among regions. The imprints on local temperature fluctuations in the KE are weak compared with other open oceans with rough topography, particularly below 2,000 m. More specifically, at around 4,000 m, the total amplitudes of temperature fluctuations can reach up to 12.23 ± 4.31 m °C (Table 4) along with evident isopycnal displacement (Table 5), which implies significant diapycnal diffusivity and mixing in the deep ocean.

We also examined 14 Deep Argo floats in the South Pacific using the same approach. Results show that the local temperature fluctuations induced by internal semidiurnal tides and near-inertial waves are prominent below 2,000 m as well, which account for 17.10 ± 9.33 m °C even at the depth of 4,000 m. Thus, we should be careful of assessing the temperature change using Deep Argo floats deployed in some deep basins where internal waves are active (Johnson et al., 2019). These high-frequency tidal signals would introduce fake signals on the Deep Argo profiles. Therefore, this may lead to overestimation/underestimation on ocean warming signals especially below 2,000 m where sufficient observations are not available.

The results derived from the deep profiling floats may also generate some uncertainties, which cannot be fully assessed at the present stage. For example, the CTDs mounted on the rapid-sampling profiling floats are SBE-37 MicroCAT CTDs, which are designed for fixed platforms like buoys/moorings. Therefore, we cannot guarantee their performance in accurately measuring the temperature on mobile platforms.

Although we have applied the moving harmonic analysis with a preferable time window of 65 points, we remain cautious to use this method due to sampling at non-fixed point. Besides, the temperature fluctuations in the SCS are a bit weak, different from the feature of prominent internal wave background. In fact, the deployment position of float #1 was far from the Luzon Strait. Therefore, more deep profiling floats together observations are greatly

needed and validated to seek the best practice for deriving internal waves signals using Deep Argo floats and to facilitate our understandings of their impact on local temperature changes.

Data Availability Statement

The Deep SOLO floats data in the East region of Australia can be downloaded from Global Argo Repository (<https://www.nodc.noaa.gov/argo/>). The deep profiling floats data and mooring data used in this study are publicly available from Figshare repository (<https://doi.org/10.6084/m9.figshare.15135705.v1>).

Acknowledgments

This research is supported by National Natural Science Foundation of China (42076009, 41527901), National Key Research and Development Program of China (2016YFC1402606), and Qingdao Pilot National Laboratory for Marine Science and Technology (2020WHZZB0101 and 2017ASTCP-ES05). Z. C. is partially supported by Fundamental Research Funds for the Central Universities (202072001) and Taishan Scholar Funds (tsqn201812022).

References

- Alford, M. H., MacKinnon, J. A., Nash, J. D., Simmons, H., Pickering, A., Klymak, J. M., et al. (2011). Energy flux and dissipation in Luzon Strait: Two tales of two ridges. *Journal of Physical Oceanography*, *41*(11), 2211–2222. <https://doi.org/10.1175/JPO-D-11-073.1>
- Alford, M. H., Peacock, T., MacKinnon, J. A., Nash, J. D., Buijsman, M. C., Centurioni, L. R., et al. (2015). The formation and fate of internal waves in the South China Sea. *Nature*, *521*(7550), 65–69. <https://doi.org/10.1038/nature14399>
- Busecke, J. J. M., & Abernathey, R. P. (2019). Ocean mesoscale mixing linked to climate variability. *Science Advances*, *5*(1), eaav5014. <https://doi.org/10.1126/sciadv.aav5014>
- Campbell, E. C., Wilson, E. A., Moore, G. W. K., Riser, S. C., Brayton, C. E., Mazloff, M. R., & Talley, L. D. (2019). Antarctic offshore polynyas linked to Southern Hemisphere climate anomalies. *Nature*, *570*(7761), 319–325. <https://doi.org/10.1038/s41586-019-1294-0>
- Chen, X., Zhang, X., Church, J. A., Watson, C. S., King, M. A., Monselesan, D., et al. (2017). The increasing rate of global mean sea-level rise during 1993–2014. *Nature Climate Change*, *7*(7), 492–495. <https://doi.org/10.1038/nclimate3325>
- Cheng, L., Abraham, J., Hausfather, Z., & Trenberth, K. E. (2019). How fast are the oceans warming? *Science*, *363*(6423), 128–129. <https://doi.org/10.1126/science.aav7619>
- Dufois, F., Hardman-Mountford, N. J., Greenwood, J., Richardson, A. J., Feng, M., & Matear, R. J. (2016). Anticyclonic eddies are more productive than cyclonic eddies in subtropical gyres because of winter mixing. *Science Advances*, *2*(5), e1600282. <https://doi.org/10.1126/sciadv.1600282>
- Durack, P. J., Wijffels, S. E., & Matear, R. J. (2012). Ocean salinities reveal strong global water cycle intensification during 1950 to 2000. *Science*, *336*(6080), 455–458. <https://doi.org/10.1126/science.1212222>
- Ferrari, R., & Wunsch, C. (2009). Ocean circulation kinetic energy: Reservoirs, sources, and sinks. *Annual Review of Fluid Mechanics*, *41*(1), 253–282. <https://doi.org/10.1146/annurev.fluid.40.111406.102139>
- Garrett, C., & Kunze, E. (2007). Internal tide generation in the deep ocean. *Annual Review of Fluid Mechanics*, *39*(1), 57–87. <https://doi.org/10.1146/annurev.fluid.39.050905.110227>
- Gill, A. E. (1982). *Atmosphere-ocean dynamics* (p. 662). Academic.
- Gleckler, P. J., Durack, P. J., Stouffer, R. J., Johnson, G. C., & Forest, C. E. (2016). Industrial-era global ocean heat uptake doubles in recent decades. *Nature Climate Change*, *6*(4), 394–398. <https://doi.org/10.1038/nclimate2915>
- Hennon, T. D., Alford, M. H., & Zhao, Z. (2019). Global assessment of semidiurnal internal tide aliasing in Argo profiles. *Journal of Physical Oceanography*, *49*(10), 2523–2533. <https://doi.org/10.1175/JPO-D-19-0121.1>
- Huang, X., Wang, Z., Zhang, Z., Yang, Y., Zhou, C., Yang, Q., et al. (2018). Role of mesoscale eddies in modulating the semidiurnal internal tide: Observation results in the northern South China sea. *Journal of Physical Oceanography*, *48*(8), 1749–1770. <https://doi.org/10.1175/JPO-D-17-0209.1>
- Jan, S., Chern, C.-S., Wang, J., & Chao, S.-Y. (2007). Generation of diurnal K1 internal tide in the Luzon Strait and its influence on surface tide in the South China Sea. *Journal of Geophysical Research*, *112*, C06019. <https://doi.org/10.1029/2006JC004003>
- Johnson, G. C., Cadot, C., Lyman, J. M., McTaggart, K. E., & Steffen, E. L. (2020). Antarctic bottom water warming in the Brazil basin: 1990s through 2020, from WOCE to deep Argo. *Geophysical Research Letters*, *47*, e2020GL089191. <https://doi.org/10.1029/2020GL089191>
- Johnson, G. C., Lyman, J. M., & Loeb, N. G. (2016). Improving estimates of Earth's energy imbalance. *Nature Climate Change*, *6*(7), 639–640. <https://doi.org/10.1038/nclimate3043>
- Johnson, G. C., Lyman, J. M., & Purkey, S. G. (2015). Informing deep Argo array design using Argo and full-depth hydrographic section data. *Journal of Atmospheric and Oceanic Technology*, *32*(11), 2187–2198. <https://doi.org/10.1175/JTECH-D-15-0139.1>
- Johnson, G. C., Purkey, S. G., Zilberman, N. V., & Roemmich, D. (2019). Deep Argo quantifies bottom water warming rates in the Southwest Pacific basin. *Geophysical Research Letters*, *46*, 2662–2669. <https://doi.org/10.1029/2018GL081685>
- Klymak, J. M., Alford, M. H., Pinkel, R., Lien, R.-C., Yang, Y. J., & Tang, T.-Y. (2011). The breaking and scattering of the internal tide on a continental slope. *Journal of Physical Oceanography*, *41*(5), 926–945. <https://doi.org/10.1175/2010JPO4500.1>
- Kobayashi, T., Amaike, K., Watanabe, K., Ino, T., Asakawa, K., Suga, T., et al. (2011). Deep NINJA: A new float for deep ocean observation developed in Japan. In *2011 IEEE symposium on underwater technology and workshop on scientific use of submarine cables and related technologies* (pp. 1–6). IEEE. <https://doi.org/10.1109/UT.2011.5774103>
- Le Reste, S., Dutreuil, V., André, X., Thierry, V., Renaut, C., Le Traon, P.-Y., & Maze, G. (2016). “Deep-Arvor”: A new profiling float to extend the Argo observations down to 4000-m depth. *Journal of Atmospheric and Oceanic Technology*, *33*(5), 1039–1055. <https://doi.org/10.1175/JTECH-D-15-0214.1>
- Levin, L. A., Bett, B. J., Gates, A. R., Heimbach, P., Howe, B. M., Janssen, F., et al. (2019). Global observing needs in the deep ocean. *Frontiers in Marine Science*, *6*, 241. <https://doi.org/10.3389/fmars.2019.00241>
- Liu, Y., Jing, Z., & Wu, L. (2019). Wind power on oceanic near-inertial oscillations in the global ocean estimated from surface drifters. *Geophysical Research Letters*, *46*, 2647–2653. <https://doi.org/10.1029/2018GL081712>
- Matthews, A. J., Singhruck, P., & Heywood, K. J. (2007). deep ocean impact of a Madden-Julian Oscillation observed by Argo floats. *Science*, *318*(5857), 1765–1769. <https://doi.org/10.1126/science.1147312>
- Munk, W., & Wunsch, C. (1998). Abyssal recipes II: Energetics of tidal and wind mixing. *Deep Sea Research Part I: Oceanographic Research Papers*, *45*(12), 1977–2010. [https://doi.org/10.1016/S0967-0637\(98\)00070-3](https://doi.org/10.1016/S0967-0637(98)00070-3)
- Racapé, V., Thierry, V., Mercier, H., & Cabanes, C. (2019). ISOW spreading and mixing as revealed by deep-Arvo floats launched in the Charlie Gibbs Fracture Zone. *Journal of Geophysical Research: Oceans*, *124*, 6787–6808. <https://doi.org/10.1029/2019JC015040>

- Rimac, A., von Storch, J.-S., Eden, C., & Haak, H. (2013). The influence of high-resolution wind stress field on the power input to near-inertial motions in the ocean. *Geophysical Research Letters*, *40*, 4882–4886. <https://doi.org/10.1002/grl.50929>
- Roemmich, D., Alford, M. H., Claustre, H., Johnson, K., King, B., Moum, J., et al. (2019). On the future of Argo: A global, full-depth, multi-Disciplinary array. *Frontiers in Marine Science*, *6*, 439. <https://doi.org/10.3389/fmars.2019.00439>
- Roemmich, D., John Gould, W., & Gilson, J. (2012). 135 years of global ocean warming between the Challenger expedition and the Argo Programme. *Nature Climate Change*, *2*(6), 425–428. <https://doi.org/10.1038/nclimate1461>
- Roemmich, D., Sherman, J. T., Davis, R. E., Grindley, K., McClune, M., Parker, C. J., et al. (2019). Deep SOLO: A full-depth profiling float for the Argo Program. *Journal of Atmospheric and Oceanic Technology*, *36*, 1967–1981. <https://doi.org/10.1175/JTECH-D-19-0066.1>
- Sun, B., Wang, S., Yuan, M., Wang, H., Jing, Z., Chen, Z., & Wu, L. (2021). Energy Flux into near-inertial internal waves below the surface boundary layer in the global ocean. *Journal of Physical Oceanography*, *51*(7), 2315–2328. <https://doi.org/10.1175/JPO-D-20-0276.1>
- Tamsitt, V., Talley, L. D., & Mazloff, M. R. (2019). A deep eastern boundary current Carrying Indian deep water South of Australia. *Journal of Geophysical Research: Oceans*, *124*, 2218–2238. <https://doi.org/10.1029/2018JC014569>
- Vic, C., Naveira Garabato, A. C., Green, J. A. M., Waterhouse, A. F., Zhao, Z., Melet, A., et al. (2019). Deep-ocean mixing driven by small-scale internal tides. *Nature Communications*, *10*(1), 2099. <https://doi.org/10.1038/s41467-019-10149-5>
- Wang, Y., Xu, Z., Yin, B., Hou, Y., & Chang, H. (2018). Long-range radiation and Interference Pattern of Multisource M_2 internal tides in the Philippine sea. *Journal of Geophysical Research: Oceans*, *123*, 5091–5112. <https://doi.org/10.1029/2018JC013910>
- Wu, L., Jing, Z., Riser, S., & Visbeck, M. (2011). Seasonal and spatial variations of Southern Ocean diapycnal mixing from Argo profiling floats. *Nature Geoscience*, *4*(6), 363–366. <https://doi.org/10.1038/ngeo1156>
- Xu, L., Li, P., Xie, S.-P., Liu, Q., Liu, C., & Gao, W. (2016). Observing mesoscale eddy effects on mode-water subduction and transport in the North Pacific. *Nature Communications*, *7*(1), 10505. <https://doi.org/10.1038/ncomms10505>
- Xu, Z., Liu, K., Yin, B., Zhao, Z., Wang, Y., & Li, Q. (2016). Long-range propagation and associated variability of internal tides in the South China sea: LONG-RANGE radiation OF K_1 and M_2 tides. *Journal of Geophysical Research: Oceans*, *121*, 8268–8286. <https://doi.org/10.1002/2016JC012105>
- Xu, Z., Wang, Y., Liu, Z., McWilliams, J. C., & Gan, J. (2021). Insight into the dynamics of the radiating internal tide associated with the Kuroshio current. *Journal of Geophysical Research: Oceans*, *126*, e2020JC017018. <https://doi.org/10.1029/2020JC017018>
- Zaron, E. D. (2019). Baroclinic tidal sea level from exact-repeat mission altimetry. *Journal of Physical Oceanography*, *49*(1), 193–210. <https://doi.org/10.1175/JPO-D-18-0127.1>
- Zhang, Z., Wang, W., & Qiu, B. (2014). Oceanic mass transport by mesoscale eddies. *Science*, *345*, 322–324. <https://doi.org/10.1126/science.1252418>
- Zhao, C., Xu, Z., Robertson, R., Li, Q., Wang, Y., & Yin, B. (2021). The three-dimensional internal tide radiation and dissipation in the Mariana Arc-trench system. *Journal of Geophysical Research: Oceans*, *126*, e2020JC016502. <https://doi.org/10.1029/2020JC016502>
- Zhao, Z. (2014). Internal tide radiation from the Luzon Strait. *Journal of Geophysical Research: Oceans*, *119*, 5434–5448. <https://doi.org/10.1002/2014JC010014>
- Zhao, Z., Alford, M. H., Girton, J. B., Rainville, L., & Simmons, H. L. (2016). Global observations of open-ocean mode-1 M_2 internal tides. *Journal of Physical Oceanography*, *46*(6), 1657–1684. <https://doi.org/10.1175/JPO-D-15-0105.1>
- Zhao, Z., & D'Asaro, E. (2011). A perfect focus of the internal tide from the Mariana Arc: A FOCUS OF internal tide. *Geophysical Research Letters*, *38*, L14609. <https://doi.org/10.1029/2011GL047909>
- Zilberman, N. V., Roemmich, D. H., & Gilson, J. (2020). Deep-ocean circulation in the Southwest Pacific Ocean interior: Estimates of the mean flow and variability using Deep Argo data. *Geophysical Research Letters*, *47*, e2020GL088342. <https://doi.org/10.1029/2020GL088342>